**TECHNOLOGY STATUS ASSESSMENT**

**SEISMIC-SCALE ROCK PHYSICS OF METHANE HYDRATE**
**CONTRACT NO. DE-FC26-05NT**

**Prepared by STANFORD UNIVERSITY**

**Prepared for US DOE – NETL**

**December 20, 2005**

**MOTIVATION FOR USE OF ROCK PHYSICS**

Gas hydrate reservoir characterization is, in principle, no different from the traditional hydrocarbon reservoir characterization. Similar and well-developed remote sensing techniques can be used, seismic reflection profiling being the dominant among them.

Seismic response of the subsurface is determined by the spatial distribution of the elastic properties and attenuation. By mapping the elastic contrast, the geophysicist can illuminate tectonic features and geobodies, hydrocarbon reservoirs included. To accurately translate elastic-property images into images of lithology, porosity, and the pore-filling phase, quantitative knowledge is needed that relates rock's elastic properties to its bulk properties and conditions. Specifically, to quantitatively characterize a natural gas hydrate reservoir, we must be able to relate the elastic properties of the sediment to the volume of gas hydrate present and, if at all possible, the permeability. One way of achieving this goal is through rock physics effective-medium modeling. By definition, and effective-medium model is a mathematical model that allows one to calculate the effective elastic and inelastic properties of a composite as well as its transport properties (e.g., permeability and electrical conductivity) from the knowledge about the component properties and their arrangement in space. Typically, an effective-medium model is based on the assumed microstructure of a composite (e.g., a granular pack versus a solid with inclusions). Also, different effective properties may require different type of modeling. For example, to calculate an elastic modulus of sand we may assume that it is a pack of elastic spheres while to estimate its permeability we may assume that it is permeated by a set of cylindrical conduits.

**HISTORY OF ROCK PHYSICS OF GAS HYDRATE**

One of the earliest semi-quantitative studies of methane hydrate accumulation is by Collins and Watkins (1985). They report an analysis of a reprocessed seismic reflection line combined with results from Deep Sea Drilling Project (DSDP) Leg 66 off the NW coast of Mexico that reveal a bottom-simulating reflector (BSR) associated with the equilibrium phase boundary of methane hydrate. Several seismic processing techniques

were used to accentuate the lateral continuity of the BSR and to delineate the top and base of a 200-700 m thick (*sic*!) concentrated hydrate layer. The authors suggest the concentrated hydrate layer extends about 20 km parallel to the slope of the inner trench wall in water depths ranging from 2.25 to 4.50 km. Direct seismic indicators, such as strong troughs in amplitude and characteristic AVO effects below the BSR as well as geochemical evidence imply small volumes of free gas may be located beneath the base of the hydrate layer. The hydrate layer sediments sealed by the presence of hydrate may serve as a seal to this free gas accumulation.

In 1986, Pearson et al. published their results of laboratory measurements of rock samples containing tetrahydrofuran hydrates. These data as well as seismic and log data from offshore methane hydrate deposits triggered attempts to theoretically describe a relation between methane hydrate concentration and seismic velocity.

All these models are based on modifications of Wyllie's time average (1956) or weighted combinations of Wyllie's time average and Wood's (1941) relation (Pearson et al., 1986; Miller et al., 1991; Bangs et al., 1993; Scholl and Hart, 1993; Minshull et al., 1994; Wood et al., 1994; Holbrook et al., 1996; Lee et al., 1996). The authors generally achieve a good fit between the data and their model by fine-tuning the input and weighting parameters required by their equations. A problem with using this technique to model marine sediments is that Wyllie's original time average equation is strictly empirical (derived from a consolidated rock database). It is not based on first-principle physics (Dvorkin and Nur, 1998) and combining Wyllie's time average with Wood's relation in a weighting scheme provides little or no physical insight. As a result, it is hard to establish a rational pattern for adapting "free" parameters to site-specific conditions.

A different, physically intuitive approach was taken by Hyndman and Spence (1992). They constructed an empirical relation between porosity and velocity for sediments without gas hydrate and approximated the effect of hydrate formation on sediment velocity by a simple reduction in porosity. By doing so they effectively assumed that hydrate becomes part of the frame without altering the frame's elastic properties.

Dvorkin and Nur (1993) suggested that the observed strong increase in the velocity due to the presence of hydrate in the sediment might be attributed to the cementing of the

3

sand grains at their contacts by the hydrate and supported this claim by a quantitative micromechanical model. However, later analysis, such as by Ecker et al. (1998) and Helgerud et al. (1999), has shown that this cementation scheme is unlikely to occur in known hydrate reservoirs.

This result was first reveled by Ecker et al. (1998) while analyzing AVO data from a BSR in the Outer Blake Ridge. The authors examined two micromechanical model that corresponded to two extreme cases of hydrate location in the pore space: (1) the hydrate cements grain contacts and strongly reinforces the sediment, and (2) the hydrate is located away from grain contacts and does not so dramatically affect the stiffness of the sediment. Only the second model could qualitatively reproduce the observed AVO response. Surprisingly, an effective-medium model that treats the sediment as a pack of elastic round grains produced reasonable results for the elastic moduli of the muddy sediment at the Outer Blake Ridge. This success of a simplified model is fairly common in the mechanics of composites where it is often not necessary to precisely reproduce the topology of a composite (in fact, such precise mimicking of natural structures is simply impossible). The main principle of a mechanician is to create a model as simple as possible but not simpler.

Later, in 1999, Helgerud et al. refined the second micromechanical model and successfully used it to reproduce the measured velocity in ODP Hole 995 and obtain hydrate concentration estimates consistent with estimates obtained from resistivity, chlorinity and evolved gas data. Once again, a simple micromechanical model that used a highly idealized representation of the actual muddy sediment produced reliable results. In 2000, Ecker et al. employed the same model to estimate the concentration of methane hydrate at the Outer Blake Ridge from marine seismic data.

It is important to mention that the quality of seismic mapping the in-situ elastic properties of sediments with methane has evolved as well as is evidenced by Xia et al. (2000). The same year, Carcione and Tinivella (2000) published an overcomplicated, hardly functional, and likely incorrect poroelastic (*sic*!) theory of sediments with methane hydrate. They used this theory to predict the elastic properties of Berea sandstone (*sic*!) with methane hydrate. This exercise was hardly relevant to methane hydrate exploration

simply because the hydrates have only been found in unlithified high-porosity sediment. Moreover, the aforementioned results were not supported by any experimental data.

The year 2000 was also marked by perhaps the first data due to Wood et al. (2000) reporting elevated P-wave attenuation in methane hydrate bearing sediment at the Outer Blake Ridge.

Lee and Collett (2001) attempted to develop a rational effective-medium theory to describe the Mallik well sonic and dipole data. Unfortunately they followed an earlier attempt by Lee et al. (1996) to use the Wyllie time average for this purpose. Wyllie's (1956) equation is only appropriate for mature consolidated sediments. Nevertheless, these authors forced the data into a physically inappropriate functional relation by using arbitrary free parameters $W$ and $n$: $V_p^{-1} = W\phi(1-S)^n V_{p1}^{-1} + [1 - W\phi(1-S)^n]V_{p2}^{-1}$, where $V_p$ is the P-wave velocity in the sediment with hydrate; $S$ is the concentration of the hydrate in the pore space; $\phi$ is the porosity of the sediment; $V_{p1}$ is the velocity computed from the three-phase Wood equation; $V_{p2}$ is the velocity from the three-phase time-average equation; and, most important, $W$ is a weighting factor and $n$ is "a constant simulating the rate of lithification with increasing gas hydrate concentration." Of course, it remains unclear how to select $W$ and $n$ if the answer ($S$ and $V_p$) is not known *a-priori*. The same year, Tinivella and Carcione used their "three-phase Biot-type theory" (*sic*!) to estimate gas hydrate saturation from the Outer Blake Ridge data. Indeed, one can easily make any problem infinitely complex. It is much more difficult to find a simple and elegant solution. Also, in 2001, Helgerud published his Ph.D. thesis on "Wave speeds in gas hydrate and sediments containing gas hydrate: A laboratory and modeling study" which for the first time reported accurate data on the elastic properties of methane hydrate obtained as a result of meticulous and painstaking laboratory work.

Lu and McMechan (2002) estimated gas hydrate saturation from the Outer Blake Ridge seismic data. This approach was very practical. They obtained a polynomial empirical relation between the impedance and hydrate saturation from log data and then used it with the seismically-derived impedance. Of course, the practical empiricism of this approach precludes its general use. Lee (2002) persisted with building up complications on top of his Wyllie-based theory by introducing yet another "Biot-

Gassmann theory for velocities of gas hydrate-bearing sediments."

The same year, a remarkable work of Guerin and Goldberg (2002) reported a counter-intuitive fact of increased signal attenuation in fast sediment with gas hydrate in the Mallik well. This observation defies the common-sense perception that a stiffer medium attenuates less. Matching results have been reported earlier at other hydrate locations offshore (Wood et al., 2000)).

Reister (2003) published a clever paper where elastic bounds are used to link hydrate concentration to the velocity. Pratt et al. (2003) analyzed cross-hole data in Mallik and discovered that the attenuation in sand with hydrate is unexpectedly large. This finding supports the 2002 result of Guerin and Goldberg on abnormal attenuation of sonic and dipole signals in Mallik. Dvorkin et al. (2003) elaborated on the rock physics model used earlier by Helgerud et al. (1999) and Ecker et al. (2000) and showed how to use this model to predict the seismic signatures of methane hydrate in different geological settings.

Matshushima (2004) discovered a similar effect in sonic data from a well drilled through a methane hydrate reservoir in Nankai Trough. This high attenuation was observed in sand with hydrate but not in surrounding shaley sediment. Dvorkin and Uden (2004) theoretically explained this counter-intuitive but experimentally consistent result. Dai et al. (2004) used the Dvorkin et al. (2004) model to map methane hydrate saturation in the Gulf of Mexico from high-resolution seismic data. The main goal of this paper was to market Schlumberger's high-resolution Q-technology.

Finally, in 2005, Bunz et al. analyzed multicomponent OBC seismic data to derive gas hydrate concentration at the Storegga Slide on the mid-Norwegian margin. They used the rock physics model of Dvorkin et al. (2003).

## ROCK PHYSICS MODELS IN PERSPECTIVE

Several attempts to construct a relation between hydrate concentration and the compressional velocity in sediments have followed the path of modifying the popular Wyllie's time average equation (1956) which states that the total travel time through rock is the volume-weighted sum of the travel times through the solid phase and the fluid

phase considered independently of each other, i.e., $V_p^{-1} = (1-\phi)V_{pS}^{-1} + \phi V_{pF}^{-1}$, where $\phi$ is the total porosity, $V_p$ is the $P$-wave velocity in the rock, and $V_{pS}$ and $V_{pF}$ are the $P$-wave velocity in the solid and in the pore-fluid phases, respectively. A qualitatively similar approach uses a weighted combination of Wyllie's time average and Wood's (1941) relation, the latter stating that the elastic modulus of a composite is the harmonic average of those of the components.

The original work of Wyllie et al. (1956) is based on laboratory measurements of ultrasonic wave propagation through a pile of alternating Lucite and aluminum disks set parallel to one another. The individual disk thickness varied between 1/16 and 1/2 inch. As expected, the total travel time through such a layered system was the sum of the travel times through Lucite and aluminum considered independently of each other. Next, by examining a large dataset of artificial and natural liquid-saturated porous samples Wyllie et al. (1956) established a remarkable and somewhat unexpected fact that the velocity data can be approximately described by the time average, as if the mineral grains and the pore space in rock were arranged in relatively thick layers normal to the direction of wave propagation.

Obviously, this is not what the pore space structure of many natural sediments appears to be, which means that Wyllie's time average is a useful and simple but physically deceptive way of summarizing extensive experimental data (as acknowledged by the authors of this equation in the original publication). Therefore, further exploiting this equation by summing up travel times through the mineral components of the solid phase and/or through the components of the pore-filling material (such as water and gas hydrate) cannot be justified by first-principle physics and thus is likely to be erroneous.

Also remember that Wyllie's time *does not work in unconsolidated sediments* (Schlumberger, 1989; Dvorkin and Nur, 1998) where apparently most of methane hydrate is concentrated. It is not based on first-principle physics and combining Wyllie's time average with Wood's relation in a weighting scheme provides little or no physical insight. As a result, it is hard to establish a rational pattern for adapting "free" parameters to site-specific conditions.

Nevertheless, various modifications of Wyllie's time average as well as weighted

combinations of Wyllie's time average and Wood's (1941) relation have found their way into gas hydrate reservoir characterization literature (Pearson et al., 1983; Miller et al., 1991; Bangs et al., 1993; Scholl and Hart, 1993; Minshull et al., 1994; Wood et al., 1994; Holbrook et al., 1996; Lee, 2002).  Generally, by fine-tuning the input parameters and weights, these equations can be forced to fit a selected dataset.  The problem with such fitting is that equations that are not based on first physical principles provide little or no physical insight.  More important, *they are not predictive* because it is difficult to establish a systematic pattern of adapting free model parameters to site-specific conditions in the exploration mode.

A different, physically intuitive approach was taken by Hyndman and Spence (1992). They constructed an empirical relation between porosity and velocity for sediments without gas hydrate and approximated the effect of hydrate formation on sediment velocity by a simple reduction in porosity.  By doing so they effectively assumed that hydrate becomes part of the frame without altering the frame's elastic properties.

Helgerud et al. (1999) further developed this idea by using a physics-based effective-medium model to quantify methane hydrate concentration from sonic and check-shot data in a well drilled through a large offshore methane hydrate reservoir at the Outer Blake Ridge in the Atlantic.  Sakai (1999) used this model to accurately predict methane hydrate concentration from well log P- and S-wave data as well as VSP data in an on-shore gas hydrate well in the Mackenzie Delta in Canada.  Ecker et al. (2000) used the same model to successfully delineate gas hydrates and map their concentration at the Outer Blake Ridge from seismic interval velocity.

This effective-medium model still includes free parameters, e.g., the coordination number (the average number of grain-to-grain contacts per grain).  Nevertheless, these free parameters have a clear physical meaning and ranges of variation as opposed to weight coefficients applied to ad-hoc selected equations in order to reconcile a model with data.  A physical effective-medium model rigorously selected to reflect the nature of the sediment under examination is *predictive* simply because its parameters can be selected in a rational and consistent way to honor the site-specific conditions, such as the effective stress, clay content, and degree of consolidation.

Essentially all of discovered natural methane hydrate is concentrated in clastic and highly unconsolidated reservoirs, either offshore or on-shore. To honor this fact we will concentrate on effective-medium models that are relevant to the nature and texture of such sediment.

## EFFECTIVE-MEDIUM MODELS FOR HIGH-POROSITY CLASTICS

The effective-medium models discussed below have two distinctive steps for constructing sediment: (a) construct the *dry-frame* of sediment and (b) place *fluid* inside this dry frame. Both steps include the computation of the bulk and shear elastic moduli ($K$ and $G$, respectively) of the sediment and its bulk density ($\rho_b$).

The latter ($\rho_b$) is simply calculated from mass balance:

$$\begin{aligned}
\rho_b &= (1-\phi)\rho_s + \phi\rho_f, \\
\rho_s &= (1-C)\rho_q + C\rho_c,
\end{aligned} \tag{1}$$

where $\phi$ is the *total* porosity; $\rho_s$ is the density of the solid (mineral) phase; and $\rho_f$ is the density of the pore fluid. $\rho_s$ is the volume-weighted average of the densities of the individual mineral components, as shown in the second line of Equation (1) for a two-mineral sediment, where $C$ is the clay content in the mineral phase and $\rho_q$ and $\rho_c$ are the densities of pure quartz and clay, respectively.

Placing the pore fluid inside the dry frame is also simple. This step uses one of the cornerstone theories of rock physics – Gassmann's (1951) fluid substitution:

$$K_{Sat} = K_s \frac{\phi K_{Dry} - (1+\phi)K_f K_{Dry}/K_s + K_f}{(1-\phi)K_f + \phi K_s - K_f K_{Dry}/K_s}, \tag{2}$$

where $K_{Sat}$, $K_{Dry}$, $K_s$, and $K_f$ are the bulk moduli of the saturated rock, dry frame, solid phase, and pore-fluid, respectively, and $\phi$ is the total porosity. The relations between the elastic moduli ($K$ and $G$), density ($\rho$), and elastic-wave velocity ($V_p$ and $V_s$) are:

$$M = \rho V_p^2, \quad G = \rho V_s^2, \quad K = M - \tfrac{4}{3}G, \tag{3}$$

where $M$ is the compressional modulus.

Let us mention for generality that Mavko et al. (1995) discovered a $V_p$–only fluid

substitution method:

$$M_{Sat} = M_s \frac{\phi M_{Dry} - (1+\phi)K_f M_{Dry}/M_s + K_f}{(1-\phi)K_f + \phi M_s - K_f M_{Dry}/M_s},$$ (4)

where $M$ (the compressional modulus) simply replaces $K$ (the bulk modulus) in the original Gassmann's equation (for fluid $M$ and $K$ are the same). We commonly use Equation (4) when conducting fluid substitution on field data simply because both $V_p$ and $V_s$ are needed to calculate the bulk modulus while the compressional modulus can be calculated from $V_p$ only which is often more reliable and accurate in field experiments.

Let us concentrate next on building the dry frame. The initial building block is a random dense pack of elastic spherical grains which is assumed to represent well-sorted sand at its maximum porosity (the critical porosity $\phi_c$). $\phi_c$ in sand may vary between 0.35 and 0.40 (Nur et al., 1998). Once again, this simple model seems to accurately mimic relevant data in sediment where the grains are certainly not identical elastic spheres. This modeling success allows us to forfeit unnecessarily complicated models where the grains are angular and irregular. Moreover, to the best of our knowledge such models are essentially nonexistent or prohibitively complicated.

The effective elastic moduli, bulk ($K_{HM}$) and shear ($G_{HM}$), of this pack can be calculated as

$$K_{HM} = \frac{n(1-\phi_c)}{12\pi R}S_N, \quad G_{HM} = \frac{n(1-\phi_c)}{20\pi R}(S_N + \frac{3}{2}S_T),$$ (5)

where $n$ is the coordination number (the average number of contacts per grain), $R$ is the average radius of the grain, and $S_N$ and $S_T$ are the normal and tangential stiffnesses, respectively, between two grains in contact. A derivation of this equation can be found in, e.g., Dvorkin (1996).

The coordination number $n$ in a sphere pack at critical porosity may vary from 5 to 9 (e.g., Dvorkin and Nur, 1996). The stiffnesses $S_N$ and $S_T$ are defined as the proportionality coefficients between the relative displacements (normal $U_N$ and tangential $U_T$, respectively) and the reaction forces ($F_N$ and $F_T$, respectively) for two individual grains in contact (Figure 1):

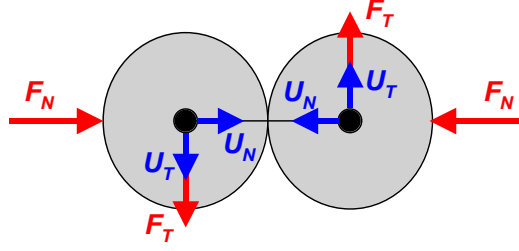$$F_N = S_N U_N, \quad F_T = S_T U_T. \tag{6}$$



Figure 1. Two individual spherical grains in contact. The normal and tangential displacements are shown in blue while the reaction forces are shown in red.

Equation (5) clearly demonstrates that the contact stiffnesses are among dominant factors that affect the elastic moduli of a grain pack. These contact stiffnesses, in turn, strongly depend on the character of the contact, specifically on whether the grains are cemented at the contact or kept together merely by the confining stress. At the same porosity, grain aggregates with cemented contacts may be much stiffer than those without cement (e.g., Dvorkin et al., 1994).

The contact stiffnesses of a pair of elastic spheres with strong friction at the contact (perfect adhesion) can be modeled according to the Hertz-Mindlin contact theory (Mindlin, 1949):

$$S_N = \frac{4aG_s}{1 - v_s}, \quad S_T = \frac{8aG_s}{2 - v_s}, \tag{7}$$

where $a$ is the radius of the contact area between the spheres. This radius is zero when no external normal forces are applied to the spheres. It monotonically increases as these forces increase. For two frictionless spheres $S_T = 0$.

The normal force $F_N$ between two spheres is related to the hydrostatic confining stress $P$ applied to the aggregate as

$$F_N = \frac{4\pi R^2 P}{n(1 - \phi_c)}. \tag{8}$$

The radius of the contact area is

$$a = \left[ F_N \frac{3(1-\nu_s)}{8G_s} R \right]^{\frac{1}{3}} = R \left[ \frac{3\pi(1-\nu_s)}{2n(1-\phi_c)G_s} P \right]^{\frac{1}{3}}. \tag{9}$$

Equations (5), (7), and (9) provide us with the final expressions for the bulk and shear moduli of a dry pack subject to confining pressure $P$ and with perfect adhesion at the contact:

$$K_{HM} = \left[ \frac{n^2(1-\phi_c)^2 G_s^2}{18\pi^2(1-\nu_s)^2} P \right]^{\frac{1}{3}}, \quad G_{HM} = \frac{5-4\nu_s}{5(2-\nu_s)} \left[ \frac{3n^2(1-\phi_c)^2 G_s^2}{2\pi^2(1-\nu_s)^2} P \right]^{\frac{1}{3}}. \tag{10}$$

For frictionless spheres, $S_T = 0$ and $S_N$ is the same as in the case of perfect adhesion. As a result, Equations (5) become

$$K_{HM} = \frac{n(1-\phi_c)}{12\pi R} S_N, \quad G_{HM} = \frac{n(1-\phi_c)}{20\pi R} S_N, \quad \frac{K_{HM}}{G_{HM}} = \frac{5}{3}, \tag{11}$$

which means that the Poisson's ratio of the dry frame of a frictionless sphere pack ($\nu_{HM}$) is constant, no matter which material the grains are made of:

$$\nu_{HM} = \frac{1}{2} \frac{(V_p/V_s)^2 - 2}{(V_p/V_s)^2 - 1} = \frac{1}{2} \left( 1 - \frac{3}{3K_{HM}/G_{HM} + 1} \right) = 0.25. \tag{12}$$

It is not constant, however, for particles with perfect adhesion. In this case

$$\frac{K_{HM}}{G_{HM}} = \frac{5(2-\nu_s)}{3(5-4\nu_s)}, \quad \nu_{HM} = \frac{\nu_s}{2(5-3\nu_s)}. \tag{13}$$

Figure 2 demonstrates that there is a large difference between the effective Poisson's ratio of a dry frictionless pack and a dry pack with perfect adhesion between the particles. In the latter case, the effective Poisson's ratio does not exceed 0.1 no matter what material the grains are made of.

For a physical pack of grains, it is virtually impossible to know in advance which fraction of the individual contacts are frictionless, i.e., $S_T = 0$, and which have perfect adhesion, i.e., $S_T = 8aG_s/(2-\nu_s)$. To account for all possibilities, we introduce an ad-hoc coefficient $f$ ($0 \le f \le 1$) and assume that

$$S_N = \frac{4aG_s}{1-\nu_s}, \quad S_T = f \frac{8aG_s}{2-\nu_s}, \tag{14}$$
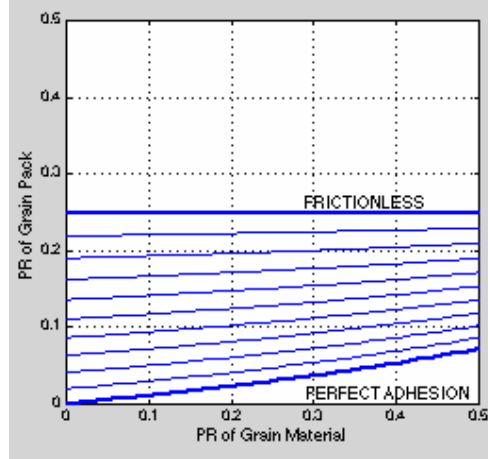
which we use instead of Equation (7).



Figure 2. Poisson's ratio of a grain pack versus that of the grain material. The upper bold curve is according to Equation (12) while the lower bold curve is according to Equation (13). The thin curves in-between are according to Equation (15) with $f$ varying between 0 and 1 with step 0.1.

The meaning of Equation (14) is that as $f$ increases from 0 to 1, the number of frictionless contacts decreases from the total number of all contacts in the pack to zero.

By combining Equations (5) and (14) instead of Equation (13) we now have

$$\frac{K_{HM}}{G_{HM}} = \frac{5(2 - \nu_s)}{3[2 + 3f - \nu_s(1 + 3f)]}, \quad \nu_{HM} = \frac{2 - 2f + \nu_s(2f - 1)}{2[4 + f - \nu_s(2 + f)]}. \tag{15}$$

The corresponding model lines for $\nu_{HM}$ with $f$ varying between 0 and 1 with step 0.1 are plotted in Figure 2. The Poisson's ratio of the dry pack gradually moves from the frictionless line down to the perfect-adhesion curve.

This model is applicable to a grain pack of fairly large porosity, the so-called "critical porosity." The next question is how to model the elastic moduli of the dry frame in the porosity range between zero and critical porosity. These moduli will obviously depend on the process that governs porosity reduction. Dvorkin and Nur (1996) discuss two modes of the pore-space geometry alteration that give rise to the same porosity reduction down form the critical porosity. One mode is the cementation of the grains where cement envelopes the original grains and by so doing reduces the total porosity. The other mode is pore-filling where small particles fill the pore space reducing the total porosity in the process.

The first, cementing, mode strongly affects the grain-to-grain contacts by reinforcing these contacts by means of additional material. The resulting increase in the elastic moduli is very large even if the porosity reduction is small (Figure 3). The second, pore-filling, mode does not strongly affect the grain-to-grain contacts although still acts to reduce porosity. The resulting increase in the elastic moduli is very modest (Figure 3).
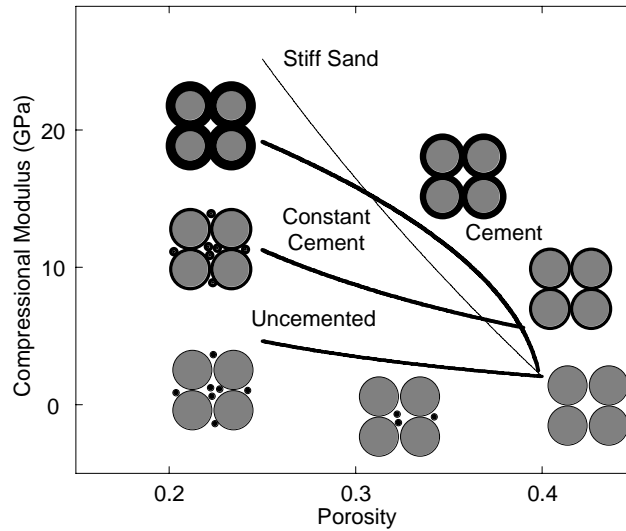


Figure 3. Compressional modulus versus porosity for three modes of porosity reduction (bold curves) for a dry pure-quartz porous system. The stiff-sand curve is shown as well.
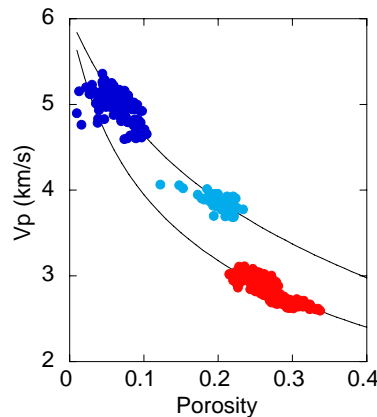


Figure 4. Velocity versus porosity in water-saturated clean sands. The symbols are from well log data, light and dark blue from cemented sand intervals, red from an unconsolidated sand interval. The lower curve is from the soft-sand model while the upper curve is from the constant-cement model (see model description below).

An intermediate (or combined) mode is the so-called "constant cement" mode

(Avseth et al., 2000). In this case, the grain pack is initially cemented to a certain degree after which cement deposition stops and the following porosity reduction is by pore-space filling. The resulting modulus-porosity curves for a dry pure-quartz porous system are plotted in Figure 3. We can see that dry porous systems of the same porosity and identical mineralogy may have drastically different elastic moduli depending on the morphology of the grain-to-grain contacts. An in-situ example from natural clean-sand reservoirs is shown in Figure 4.

We concentrate here on the uncemented (also called "soft-sand") model which is of special interest in methane hydrate exploration. This analytical model uses two end-points in the modulus-porosity plain: one at the critical porosity where the dry-frame elastic moduli are calculated according to Equations (5), (9), and (14) and the other at zero porosity where the elastic moduli is simply those of the solid-phase material. These two end-points are connected by curves that have the functional form of the lower Hashin-Shtrikman bound (Dvorkin and Nur, 1996):

$$
\begin{aligned}
K_{Dry} &= [\frac{\phi/\phi_c}{K_{HM} + \frac{4}{3}G_{HM}} + \frac{1-\phi/\phi_c}{K_s + \frac{4}{3}G_{HM}}]^{-1} - \frac{4}{3}G_{HM}, \\
G_{Dry} &= [\frac{\phi/\phi_c}{G_{HM} + Z} + \frac{1-\phi/\phi_c}{G_s + Z}]^{-1} - Z, \quad Z = \frac{G_{HM}}{6}\left(\frac{9K_{HM} + 8G_{HM}}{K_{HM} + 2G_{HM}}\right),
\end{aligned}
\tag{16}
$$

where $\phi$ is the total porosity and the elastic moduli of the solid-phase material are calculated from those of the components according to Hill's (1952) average:

$$
K_s = \frac{1}{2}[\sum_{i=1}^{m} f_i K_i + (\sum_{i=1}^{m} f_i/K_i)^{-1}], \quad G_s = \frac{1}{2}[\sum_{i=1}^{m} f_i G_i + (\sum_{i=1}^{m} f_i/G_i)^{-1}],
\tag{17}
$$

where $m$ is the number of mineral constituents; $f_i$ is the volumetric fraction of the $i$-th constituent in the solid phase; and $K_i$ and $G_i$ are the bulk and shear moduli of the $i$-th constituent, respectively. The solid-phase material density is calculated as

$$
\rho = \sum_{i=1}^{m} f_i \rho_i,
\tag{18}
$$

where $\rho_i$ is the density of the $i$-th constituent.

The constant-cement model is essentially the same model but with the high-porosity

end-point lying on the cement-model curve (Figure 3).

A counterpart set of equations are the "stiff-sand" equations which use the same end-points but instead of using the lower Hashin-Shtrikman bound functional form to connect these end-points employs the upper Hashin-Shtrikman bound. It is shown in Figure 3 as a thin curve. The corresponding equations are:

$$
K_{Dry} = [\frac{\phi/\phi_c}{K_{HM} + \frac{4}{3}G_s} + \frac{1-\phi/\phi_c}{K_s + \frac{4}{3}G_s}]^{-1} - \frac{4}{3}G_s,
$$

$$
G_{Dry} = [\frac{\phi/\phi_c}{G_{HM} + Z} + \frac{1-\phi/\phi_c}{G_s + Z}]^{-1} - Z, \quad Z = \frac{G_s}{6}\left(\frac{9K_s + 8G_s}{K_s + 2G_s}\right).
$$

(17)

## APPLICATION OF MODELS TO SAND WITH HYDRATE

Let us now apply some of the models discussed in the previous section to high-porosity brine-saturated clean (100% quartz) sand that contains methane hydrate in the pore space and, possibly, free gas. The elastic moduli and densities of the components of this system are listed in Table 1.

Table 1. Elastic moduli and density of rock and fluid components.

| Component | Bulk Modulus (GPa) | Shear Modulus (GPa) | Density (g/cc) |
|---|---|---|---|
| Quartz | 36.60 | 45.00 | 2.650 |
| Clay | 21.00 | 7.00 | 2.580 |
| Brine | 2.330 | 0.00 | 1.029 |
| Gas | 0.017 | 0.00 | 0.112 |
| Methane Hydrate | 7.40 | 3.30 | 0.910 |

Consider a clean sand pack at its critical porosity. The pore space of the sand is filled with brine. The methane hydrate that we place in the pore space of the sand replaces part of the brine. We will explore three types of hydrate arrangement in the pores (Figure 5): (a) hydrate acts as contact cement; (b) hydrate acts as a pore-filling component of the mineral frame and affects the total porosity and properties of the frame; and (c) hydrate is suspended in the brine without interacting with the mineral frame, i.e., it becomes part of the pore fluid and only affects its density and bulk modulus.
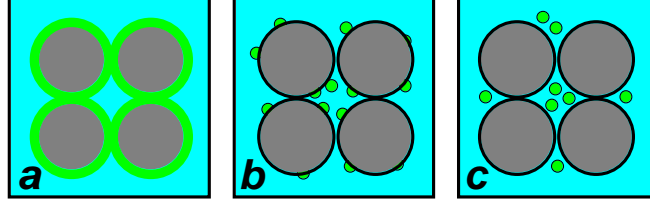
16

Figure 5. Three types of methane hydrate arrangement in the pore space. From left to right – (a) hydrate as contact cement; (b) non-cementing hydrate as part of the mineral frame; and (c) hydrate as part of the pore fluid. The quartz grains are gray; brine is cyan; and hydrate is green.

The hydrate saturation of the pore space ($S_h$) is often the quantity used to characterize a natural methane hydrate reservoir. If the total porosity of the hydrate-bearing sand is $\phi_c$, the volumetric concentration of hydrate in a unit volume of rock ($C_h$) is $\phi_c S_h$. In both cementing and non-cementing cases (the first two frames in Figure 5), the hydrate will be treated as part of the mineral phase. Therefore, the total porosity of the sand with hydrate ($\bar{\phi}$) is

$$\bar{\phi} = \phi_c - C_h = \phi_c(1 - S_h). \qquad (18)$$

$\bar{\phi}$ becomes $\phi_c$ for $S_h = 0$ and zero for $S_h = 1$.

In the case where the hydrate is treated as part of the pore fluid, the total porosity of the mineral frame does not change as $S_h$ varies and remains constant $\phi_c$. Instead, the bulk modulus and density of the pore fluid that is now a mixture of brine and hydrate vary. The bulk modulus of this mixture ($\bar{K}_f$) is the harmonic average of those of hydrate ($K_h$) and brine ($K_f$):

$$\bar{K}_f = \left[ \frac{S_h}{K_h} + \frac{1 - S_h}{K_f} \right]^{-1}, \qquad (19)$$

while its density ($\bar{\rho}_f$) is the arithmetic average of those of hydrate ($\rho_h$) and brine ($\rho_f$):

$$\bar{\rho}_f = S_h \rho_h + (1 - S_h)\rho_f. \qquad (20)$$

The results of calculating the elastic-wave velocity using these three models are displayed in Figure 6. Also displayed in this figure are data from a methane hydrate exploratory well. Apparently, model "b" in which the hydrate is assumed to be a non-cementing components of the mineral frame matches the data best.
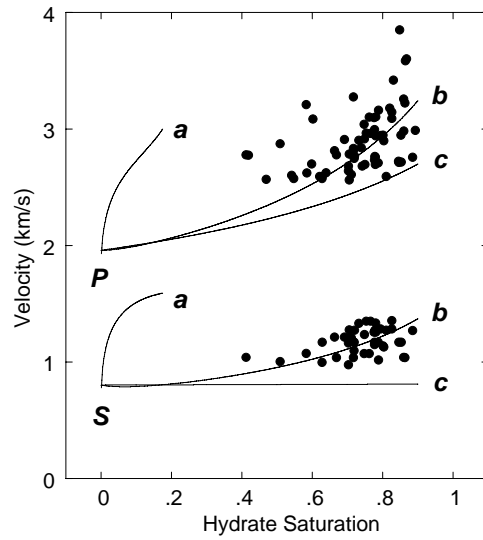
17

Figure 6. P- and S-wave velocity versus methane hydrate saturation in a quartz-sand-brine-hydrate system. The curves are marked with letters that match the three cases of position in the pore space shown in Figure 5. The upper set of curves is for the PS-wave velocity while the lower set is for the S-wave velocity. The symbols are log data from a methane hydrate exploratory well.
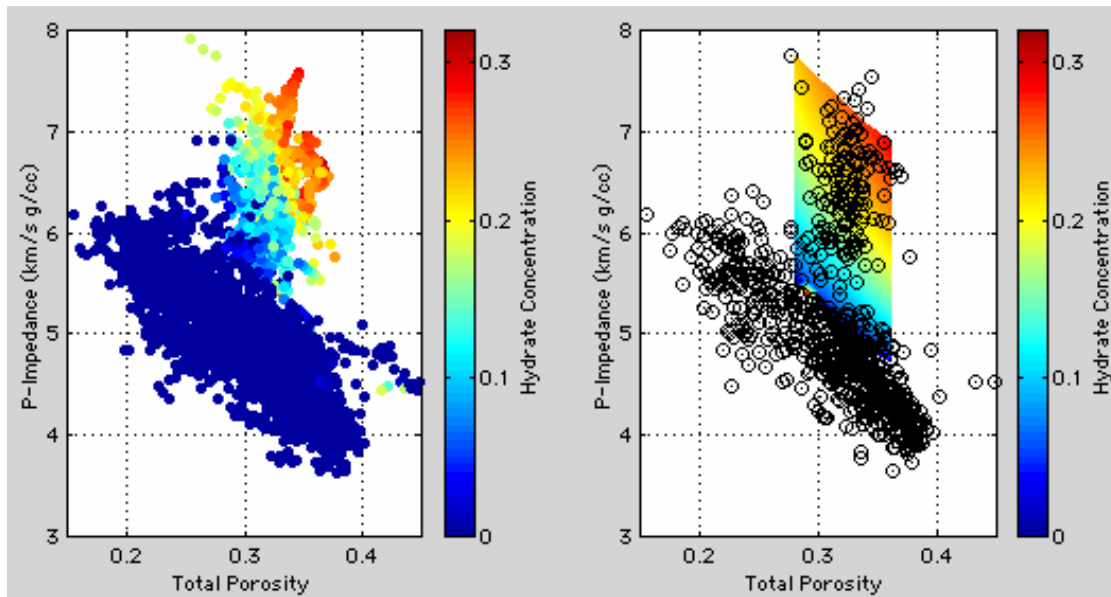


Figure 7. Left -- impedance versus the sediment's total porosity in on-shore well Mallik 2L-38, color-coded by hydrate concentration (hydrate saturation times the sediment's porosity). Right -- the same data (every fifth point) shown as empty black circles on the background of the modeled impedance strip. The model uses the hydrate arrangement "b" (the hydrate is a non-cementing part of the sediment frame). The modeled impedance is color-coded by hydrate concentration.

Another strong argument in favor of using model "b" is that field data typically indicate that both P- and S-wave velocity increase with increasing methane hydrate saturation. This fact helps us refute model "b" because if methane hydrate is assumed to be part of the pore fluid, no increase of the S-wave velocity due to the presence of hydrate in the pore space can be theoretically obtained.

Essentially all previous studies that used these effective-medium models to model field log and seismic data (Helgerud et al., 1999; Sakai, 1999; Ecker et al., 2000; Dvorkin et al. 2003; Dvorkin et al., 2003; Dai et al., 2004) arrived at the same conclusion.

Dvorkin and Uden (2004) applied this model to well data from the Mallik on-shore exploratory methane hydrate well. The model accurately delineates the sands with hydrate from water-saturated sand and shale without hydrate (Figure 7).

## APPLICATION OF MODELS TO NANKAI TROUGH WELLS

In this section we apply the rock physics methane hydrate model established above to two exploratory wells in Nankai trough – MITI-1 and MITI-2. The wireline data from these two wells are displayed in Figure 8. The hydrate occurs in the sandy parts of the wells (low GR) and is characterized by elevated P- and S-wave velocity.

In Figure 9 we cross-plot the P- and S-wave velocity versus the total porosity of the sediment for MITI-1 and superimpose model curves on top of these cross-plots. The model curves are calculated for clean sand without methane hydrate as well as the same sand with 0.3, 0.6, and 0.9 hydrate saturation. In addition, we calculate the curves for water-saturated sediment with 0.5 and 1.0 clay content and sediment with free gas. The model curves accurately match the data, including the small interval with free gas at the base of methane hydrate.

The same display is given for MITI-3 in Figure 10. These result further validate the applicability of our rock physics model in Nankai Trough.

To further illustrate the applicability of the rock physics model to the Nankai Trough environment, we cross-plot the velocity versus hydrate saturation in Figure 11 with model lines on top. The model accurately matches the data.
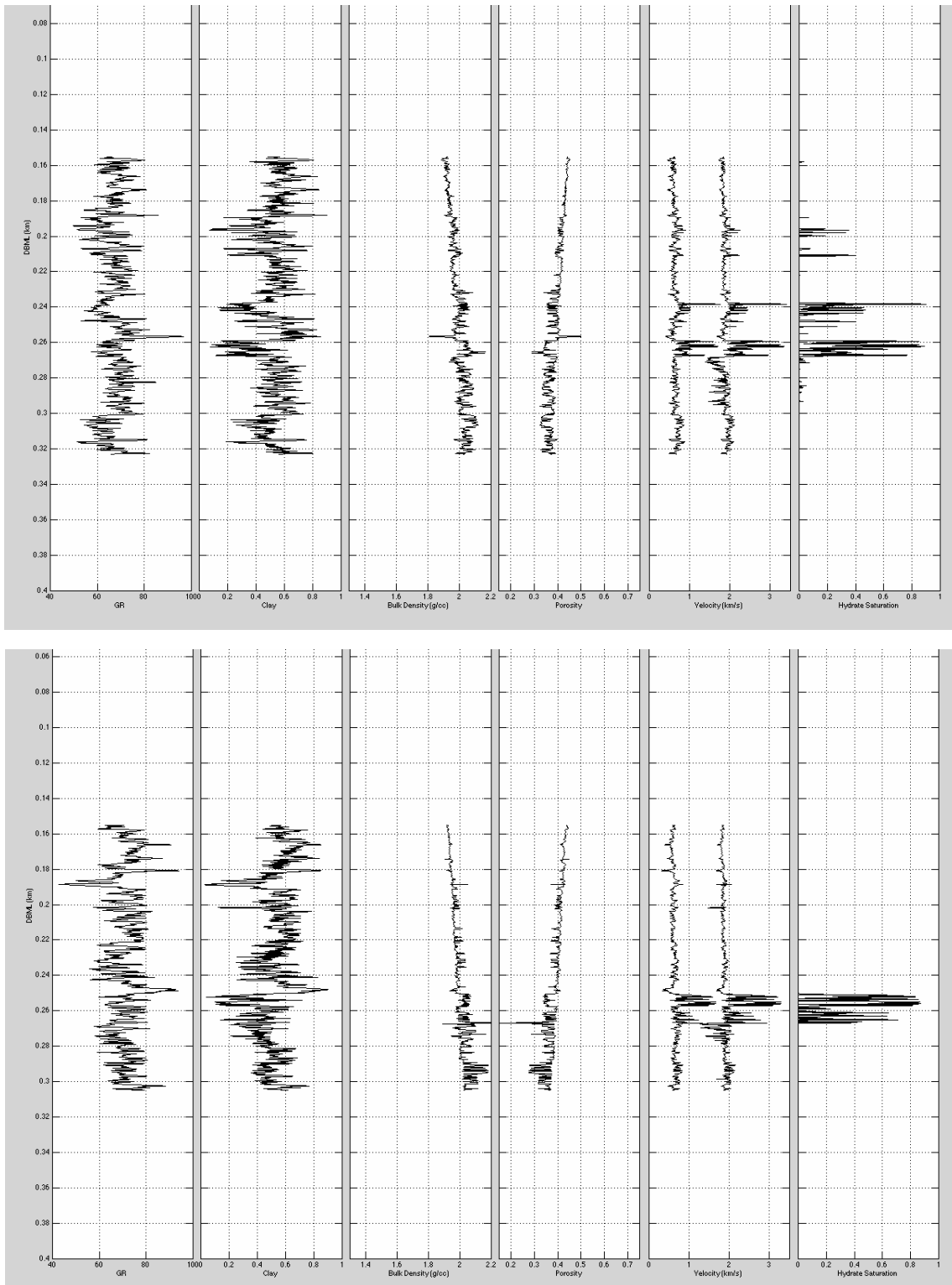
Figure 8. Wireline curves for well MITI-1 (top) and MITI-3 (bottom). From left to right – GR; clay content; bulk density; total porosity; P- and S-wave velocity; and hydrate saturation calculated from density.
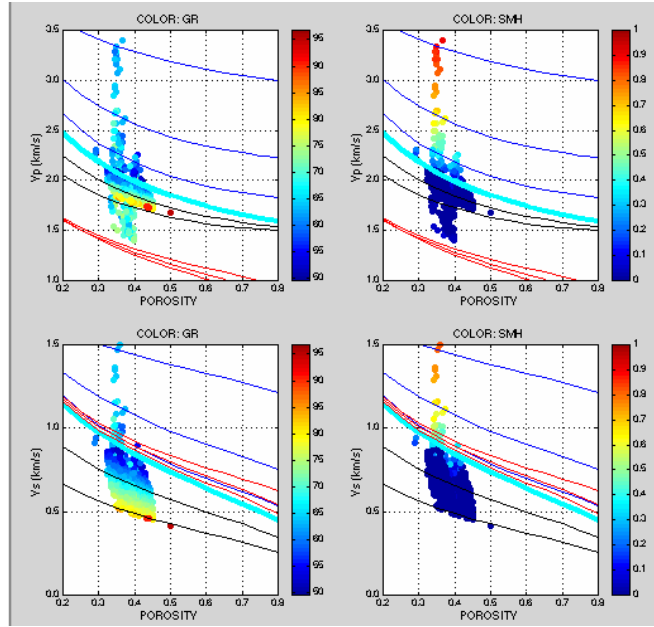
Figure 9.  Velocity-porosity cross-plots for MITI-1.  The upper row is for the P-wave velocity while the lower row is for the S-wave velocity.  The data points are color-coded (from left to right) by GR and methane hydrate saturation calculated from resistivity.  The bold cyan model curve is the baseline drawn for brine-saturated clean sand.  The black curves below the baseline are for brine-saturated shale with clay content 0.5 and 1.0.  The red curves are for gas-saturated clean sand with gas saturation ranging from 0.2 to 0.8.  The blue curves above the baseline are for clean sand with methane hydrate saturation 0.3; 0.6; and 0.9.
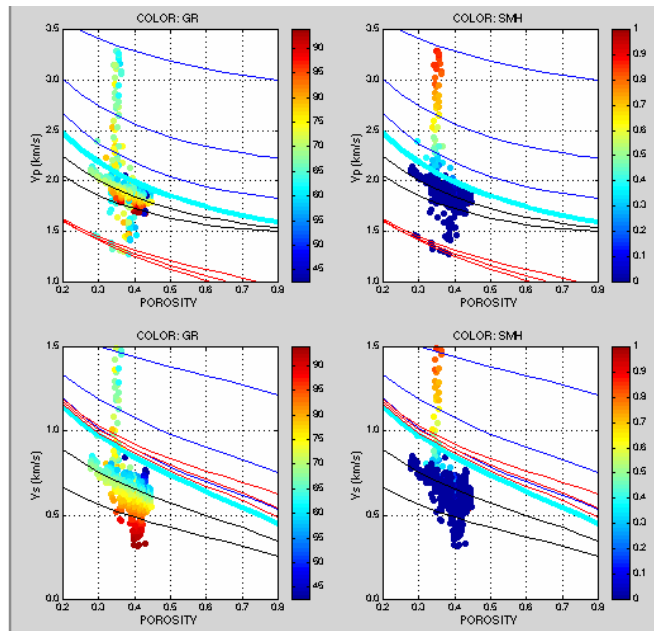


Figure 10.  Velocity-porosity cross-plots for MITI-3.  The display is the same as in Figure 9.
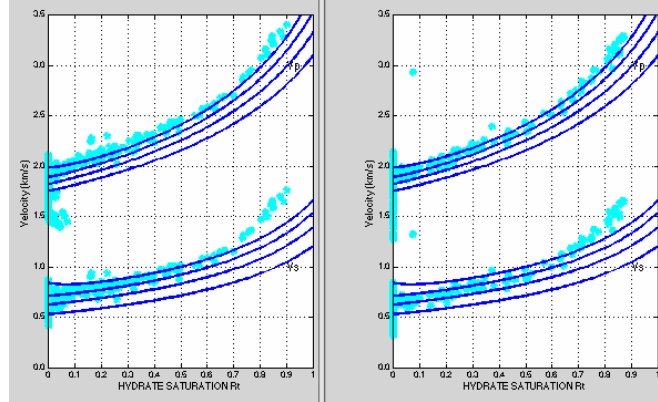
21

Figure 11.  Velocity-hydrate-saturation cross-plots for MITI 1 (left) and MITI 3 (right).  The model curves are from the rock physics model for zero; 0.3; 0.6; and 0.9 clay content (from bottom to top).

## USING ROCK PHYSICS IN PREDICTIVE MODE

Once a rock physics gas hydrate model (GHM) has been established and validated by data, it can be used in a predictive mode to assess the seismic signature of methane hydrate away from well control in "what-if" mode.

For example in Figure 12 we use GHM is used to predict the elastic properties of sand with porosity ranging from 20 to 40% filled with solid methane hydrate with the hydrate saturation in the pore space ranging from zero to 100%.  The rest of the pore space is filled with brine.  The assumed mineralogy is 90% quartz and 10% clay.  The results shown in Figure 12 indicate that the larger the gas hydrate concentration at fixed porosity the larger the P-wave impedance and the smaller the Poisson's ratio (PR).  The two plots shown in Figure 12 can be used to extract both the total porosity and gas hydrate concentration from elastic well log or impedance inversion data.

The net amount of the hydrate in a unit volume of rock (hydrate concentration in rock), which is likely to be the ultimate goal of gas hydrate exploration, is the product of the total porosity and gas hydrate saturation of the pore space.  This quantity is modeled and plotted versus the P-wave impedance and Poisson's ratio in Figure 13 for a sand with 10 and 20% clay content.  Small variations of clay content in hydrate-bearing sand do not dramatically change the range of elastic attributes within which high gas hydrate concentration can be found.  Large amount of clay may simply preclude the formation of hydrate in the sediment because the methane gas may not be able to enter such sediment

22

to form hydrate due to the sediment's low permeability associated with large clay content. These ranges for PR and P-wave impedance are 0.31 to 0.33 and 7 to 9 km/s g/cc, respectively.
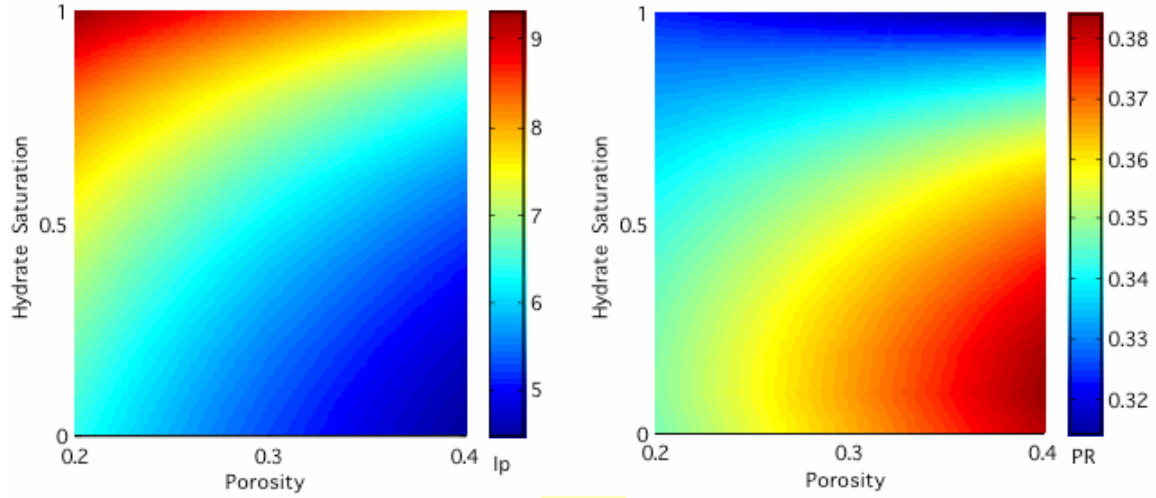


Figure 12. P-wave impedance in km/s g/cc (left) and Poisson's ratio (right) versus porosity and gas hydrate saturation of the pore space in water-saturated sand with 10% clay content. Color coding is by the impedance (left) and Poisson's ratio (right).
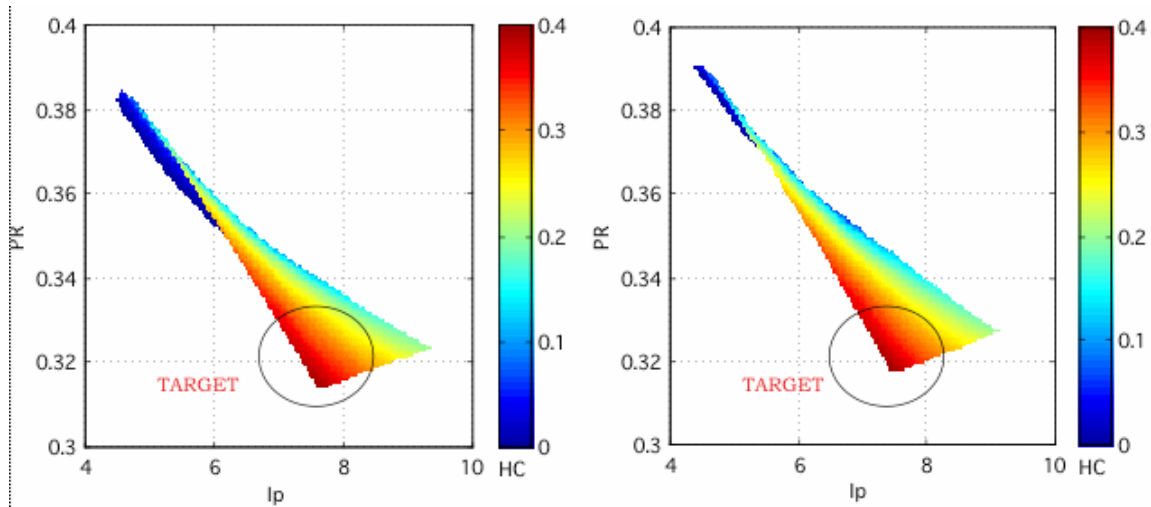


Figure 13. Hydrate concentration in rock (the color code) versus the P-wave impedance (in km/s g/cc) and Poisson's ratio for water-saturated sand with 10% (left) and 20% (right) clay content. The color coding is by the hydrate concentration. Highest hydrate concentration domains are encircled in both frames.

The rock physics model used here helps discriminate sediments with commercial gas hydrate concentration from the background water saturated rock and sands with free gas

in the elastic attribute space. In Figure 14 (left) the sand-with-hydrate domain in the impedance-PR plane is color-coded by hydrate concentration in the rock while the sand-with-free-gas domain is colored yellow and the sand/shale-with-water domain is colored cyan. The target, sand with a large hydrate concentration, is characterized by a relatively high impedance and medium-to-high PR. The same model data but displayed in the $V_p - V_p/V_s$ domain are shown in Figure 14, right.
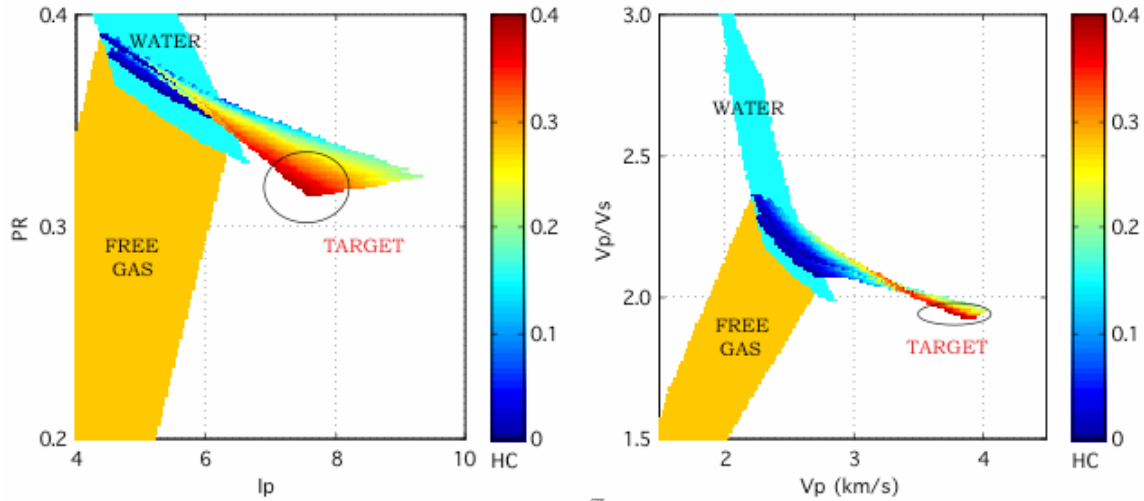


Figure 14. Hydrate concentration in rock (HC) versus the P-wave impedance and Poisson's ratio (left) and the P-wave velocity and Vp/Vs ratio (right). The cases displayed include sand with gas hydrate with clay content 10% and 20%; water-saturated sand with clay content between zero and 100%; and sand with free gas with clay content 10% and 20%. The data for sand with gas hydrate are color-coded by hydrate concentration in rock. The data for sand with free gas are colored yellow while the data for water-saturated sand are colored cyan.

Consider finally a vertical section of earth where a dipping sand layer is encased in shale (Figure 15). The shale is fully saturated with water. The upper part of the sand layer is partially saturated with methane hydrate with the hydrate saturation of the pore space about 50%. The lower part of the sand contains free methane gas with about 20% gas saturation. Such arrangement of methane hydrate and free gas is likely in sea-bottom sediment where the hydrate-gas contact position corresponds to the lower boundary of the stability zone of methane hydrate. In several documented cases, a strong impedance contrast is observed between the sediment with hydrate and the underlying sediment with free gas. This contrast gives rise to a strong seismic reflection known as the bottom-

simulating reflector (BSR).

The elastic properties of the sediment in the vertical pseudo-section under examination are calculated according to the above-described GHM model. The modeled P-wave impedance and Poisson's ratio are displayed in Figure 15.

As expected, there is a strong impedance contrast between the sand with gas hydrate and the sand with free gas. The impedance in the sand with gas hydrate is also much larger than that in the shale. This large impedance may serve as an indicator of hydrate-cemented sand in a shallow marine environment usually composed of very soft sediments.

Poisson's ratio (PR) that can be obtained from elastic impedance inversion is useful as a free gas indicator. PR in the sand with free gas falls below 0.2 while that in the sand with gas hydrate and in the shale exceeds 0.3. Also, PR in the hydrate-cemented sand is smaller than in the shale background and should be expected to be smaller than in water-saturated sand without gas hydrate Therefore, PR, in addition to the impedance, can serve as an indicator of hydrate-cemented sand.
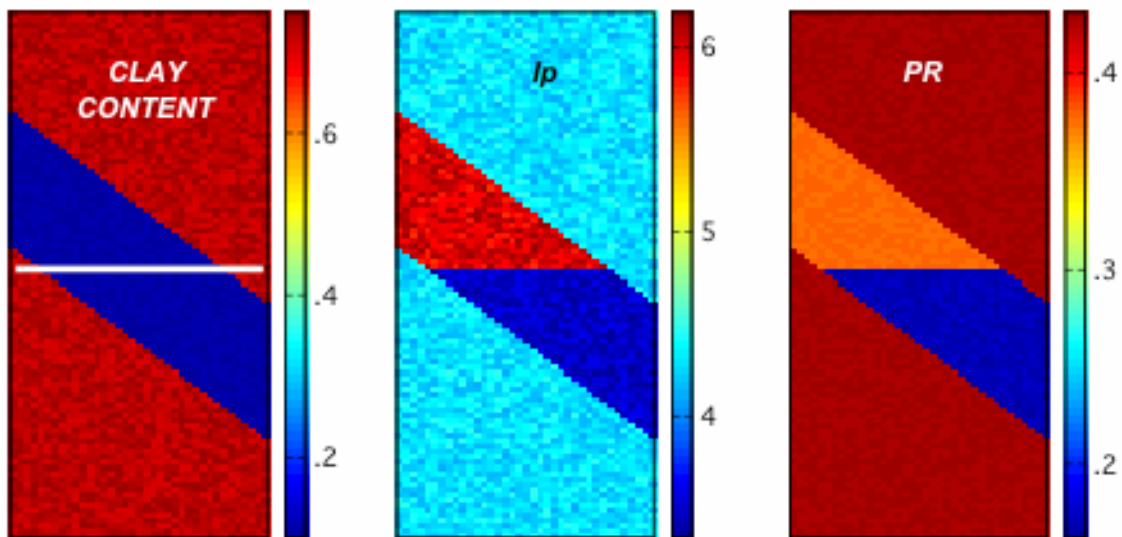


Figure 15. Pseudo-section of earth with a dipping sand layer encased in shale. From left to right --clay content (small in the sand and large in the shale), the horizontal white bar indicates the hydrate-free gas contact; P-wave impedance in km/s g/cc; and Poisson's ratio.

The ultimate goal of rock physics modeling presented here is to determine gas hydrate saturation of the pore space from seismic data. We have established that there is

a strong relation between the P-wave impedance and the amount of hydrate in the pore space. Therefore, impedance inversion is an appropriate technique for gas hydrate reservoir characterization.

Unfortunately, there are multiple factors that affect the elastic properties of sand with hydrate. Some of them, such as the bulk modulus and density of the pore fluid, and the differential pressure, are relatively easy to bound. The remaining factors, porosity, clay content, and gas hydrate saturation are impossible to uniquely determine from the acoustic impedance. However, model-driven bounding can help bracket the results.

Assume, for example, that the total porosity of a hydrate-cemented sand body may vary between 20 and 30% and the clay content may vary between 5 and 15%. Then model-derived nomograms shown in Figure 16 can provide a reasonably narrow range of hydrate saturation from impedance. For example, if the measured impedance is 7 km/s g/cc then the hydrate saturation lies between 45 and 80%. This degree of narrowing uncertainty is realistically achievable. It can only be further reduced by imposing additional stringent assumptions on reservoir properties.



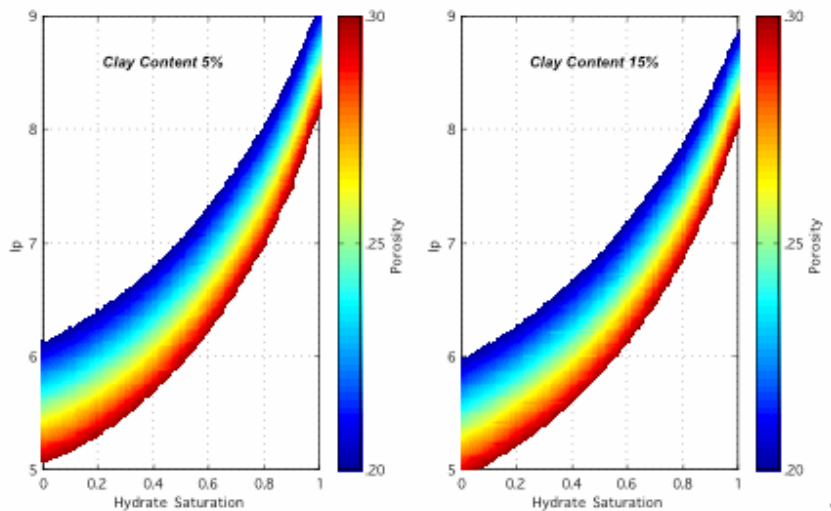Figure 16. Model-derived P-wave impedance (km/s g/cc) versus hydrate saturation color-coded by the total porosity. Left: 5% clay content. Right: 15% clay content.

Even further reduction of uncertainty in gas hydrate reservoir characterization is probably possible if seismic attributes other than the acoustic impedance, such as Poisson's ratio and attenuation, can be accurately measured from field data. Once again,

26

the model-driven approach is paramount for bracketing the results.

## ATTENUATION IN METHANE HYDRATE RESERVOIR

Elastic-wave data collected in sediments with methane hydrate around the world point to significant velocity increase due to the presence of the hydrate in the pores. This effect can be easily understood if we recall that gas hydrate is a solid as opposed to brine or gas. By filling the pore space, gas hydrate acts to reduce the porosity available to the pore-fluid and, by so doing, increase the elastic moduli of the solid frame. It is difficult to reconcile this effect with more recent observations that the attenuation of elastic waves grows with increasing gas hydrate concentration.

Indeed, intuitively, one would expect that the stiffer the rock the smaller the relative elastic energy losses per cycle and, therefore, the smaller the attenuation. Measurements in many sediments support this intuition. For example, Klimentos and McCann (1990) show that attenuation increases with increasing porosity and clay content while the velocity behaves in an opposite way. Recent results by Koesoemadinata and McMechan (2001) who statistically generalized many experimental data point to the same fact. This intuition, combined with quantitative modeling, led Dvorkin et al. (2003) to suggest reduced absorption as a possible seismic attribute for methane hydrate detection.

However, the facts are persistent. Unexpectedly large attenuation in sediments with gas hydrates has recently been observed at different geographical locations, in different depositional environments, and at different frequencies. In 1999, Guerin et al. presented qualitative evidence of dipole waveform attenuation in the hydrate-bearing sediments in the Outer Blake Ridge. Sakai (1999) noted that the shear-wave VSP signal may be strongly attenuated in a Mallik well within the methane-hydrate interval. Wood et al. (2000) observed increased attenuation of seismic waves at the same location. Guerin and Goldberg (2002) used monopole and dipole waveforms to quantify compressional- and shear-wave attenuation. They reported a monotonic increase in both with increasing hydrate saturation. Pratt et al. (2003) reported an increase in attenuation in the Mallik hydrate reservoir between two methane hydrate wells during cross-hole experiments in the 150 to 500 Hz frequency range. Anomalous absorption has been observed in the

Nankai Trough methane hydrate reservoir in the seismic frequency range (M.T. Taner, personal communication). We have no reason to question the validity of these field data and, therefore, concern ourselves with the task of establishing a plausible quantitative physical explanation and, by so doing, determine in which situations increased attenuation can be expected in methane hydrate reservoirs.

Seismic energy in porous rock with fluid dissipates due to wave-induced oscillatory cross-flow. The viscous-flow friction irreversibly transfers part of the energy into heat. This flow may be especially strong in partially-saturated rock where the viscous fluid phase (water) moves in and out of the gas-saturated pore space.

Such viscous-friction losses may also occur in wet rock where elastic heterogeneity is present. Deformation due to a stress wave is relatively strong in the softer portion of the rock and weak in the stiffer portion. The spatial heterogeneity in the deformation of the solid frame forces the fluid to flow between the softer and stiffer portions. Such cross-flow may occur at all spatial scales.

Microscopic "squirt-flow" is developed at the sub-millimeter pore scale because a single pore may include compliant crack-like and stiff equi-dimensional parts. Macroscopic "squirt-flow" which is more relevant to the seismic prospecting scale, may occur due to elastic heterogeneity in the rock frame elastic moduli. This mechanism has recently received a rigorous mathematical treatment by Pride et al. (2003) in a "double-porosity" model.

"Squirt flow" is a term commonly used in poroelasticity to allude to the oscillatory fluid flow due to compression and extension of the rock frame caused by a propagating stress wave.

However, there is a simple way of quantifying the effect of macroscopic "squirt-flow" on seismic wave attenuation. Recall that in a viscoelastic body causality requires that there be a very specific relation between attenuation and frequency-related velocity (or elastic modulus) change. This relation is referred to as the Kramers-Kronig equation. It implies that a larger attenuation generally is associated with a larger wave-speed change between low frequency and high frequency. It has an especially simple expression in a standard linear solid: $2Q_{Max}^{-1} = (M_H - M_L)/\sqrt{M_H M_L}$, where $Q_{Max}^{-1}$ is the

maximum inverse quality factor (the ratio of the elastic energy dissipated per cycle of oscillation to the peak elastic energy during the cycle); $M_H$ is the compressional modulus at very high frequency; and $M_L$ is the compressional modulus at very low frequency. The compressional modulus is defined as the product of the bulk density and P-wave velocity squared.

Consider now a model rock that is fully water-saturated (wet) and has two parts. One part (80% of the rock volume) is shale with porosity 0.4; clay content 0.8 (the rest is quartz); and the P-wave velocity 1.9 km/s. The other part (the remaining 20%) is clean high-porosity slightly-cemented sand with porosity 0.3 and the P-wave velocity 3.4 km/s. The compressional modulus is 7 GPa in the shale and 25 GPa in the sand. Because of the difference between the compliance of the sand and shale parts, their deformation due to a passing wave is different, leading to macroscopic "squirt-flow."

At high frequency, there is essentially no cross-flow between sand and shale simply because the flow cannot fully develop during the short cycle of oscillation. The effective elastic modulus of the system is the harmonic (Backus) average of the moduli of the two parts: $M_H = 16$ GPa.

At low frequency, the cross-flow can easily develop. In this case, the fluid reacts to the combined deformation of the dry frame of the sand and shale. The dry-frame compressional modulus in the shale is 2 GPa while that in the sand is 20 GPa. The dry-frame modulus of the combined dry frame – 7 GPa – is the harmonic average of the two. The arithmetically averaged porosity of the model rock is 0.32. To estimate the effective compressional modulus of the combined dry frame with water we theoretically substitute water into this combined frame. The result is $M_L = 13$ GPa. The calculated maximum inverse quality factor is $Q_{Max}^{-1} = 0.12$ which translates into a noticeable attenuation coefficient of about 0.02 dB/m. The above-described averaging technique for attenuation estimate in wet rock can be applied to well log curves by means of a moving averaging window.

We apply this attenuation modeling to well log data from the Mallik 2L-38 well drilled in Canada in Mackenzie River Delta. The interval under examination includes several low-GR sand bodies whose pore space is partly filled with methane hydrate

(Figure 17). The rock-frame porosity in these sands exceeds 30% and the measured P-wave impedance is much larger than in the surrounding shale or sand without hydrate. This impedance contrast gives rise to strong elastic heterogeneity in the interval. The impedance data can be accurately matched by GHM (Figure 7).

For the purpose of attenuation calculation, the sediment in the interval is considered wet because it does not contain free gas. Then the methane hydrate has to be treated as part of the sediment's frame. Of course, where the hydrate is present, the porosity of this modified frame is smaller than that of the original frame composed of quartz and clay and equals the product of the original porosity and one minus methane hydrate saturation. Also, the effective solid-phase modulus of the modified frame has to include the component due to methane hydrate. The pore fluid in this modified frame is water.
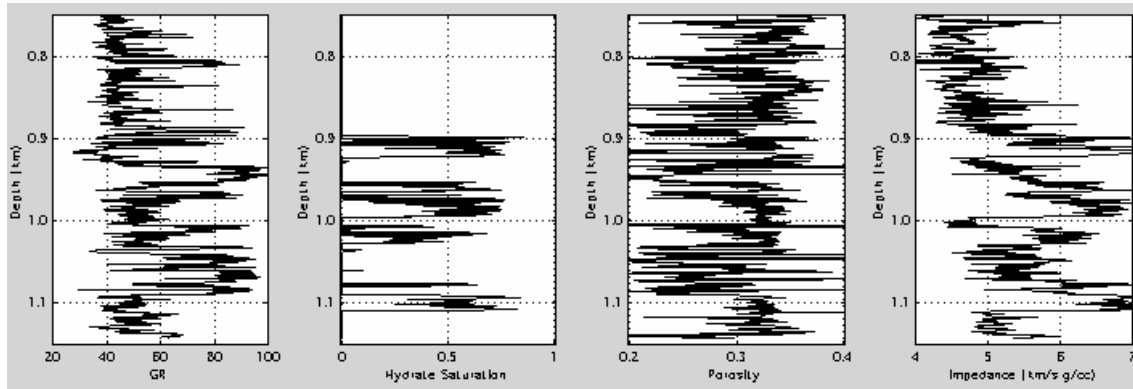


Figure 17. Well log curves in Mallik 2L-38. From left to right, gamma-ray, methane hydrate saturation of the pore space, porosity of the sediment frame (without hydrate), and the P-wave impedance.

We estimate attenuation from scattering in the entire interval of Mallik 2L-38. $Q^{-1}$ thus calculated appears as a single number for the entire interval because scattering attenuation is a layer property. The result (Figure 19) indicates that although the scattering attenuation is smaller than the macroscopic squirt flow attenuation, it has the same order of magnitude and has to be taken into account when estimating the total attenuation of elastic waves in sediments with methane hydrate.

Figure 18. Well log curves in Mallik 2L-38 with calculated inverse quality factor shown in red.

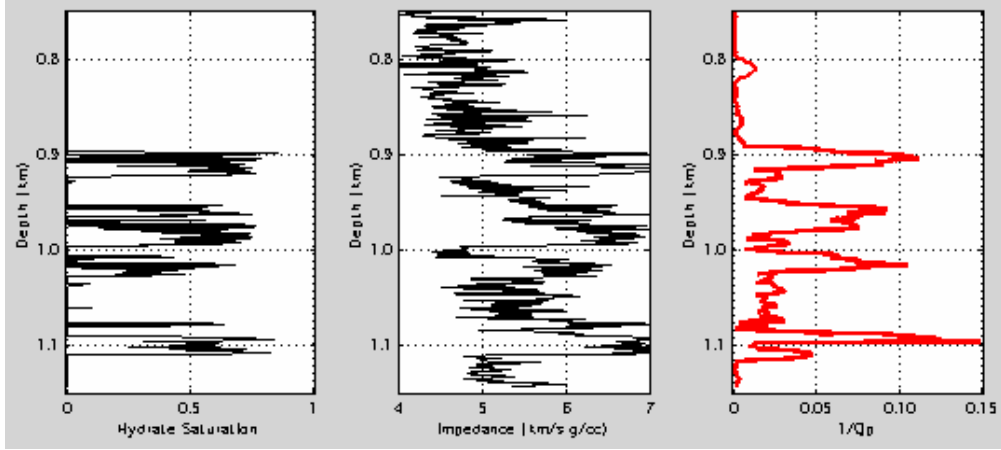The result of our inverse quality factor estimation is shown in Figure 18. High attenuation occurs precisely where methane hydrate is present, the impedance contrast is large, and elastic heterogeneity is strong. Our attenuation estimates quantitatively explain the observations that the amplitude loss is high in sediments with methane hydrate. The inverse quality values are not that different from the recent in-situ estimates of Pratt et al. (2003) obtained from cross-hole waveform inversion data in a 150 to 500 Hz frequency range. Those cross-hole data give $Q^{-1}$ between 0.15 and 0.20 in the sands with methane hydrate and very small (less than 0.05) in the rest of the section.

The self-induced elastic heterogeneity in a methane hydrate reservoir may also cause scattering attenuation. To estimate this contribution we use the O'Doherty-Anstey formula $Q^{-1} = 2\pi f \hat{I}(2f)$, where $f$ is frequency and $\hat{I}$ is the power spectrum of the logarithmic impedance fluctuations of the medium $\ln(I_p) - \langle \ln(I_p) \rangle$.
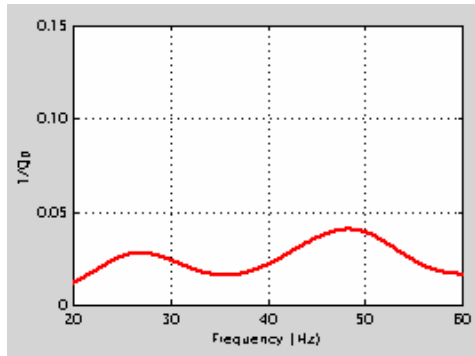


Figure 19. The inverse quality factor due to scattering in Mallik 2L-38

## CAVEATS DUE TO SEISMIC RESOLUTION

Rock physics model are usually utilized on a point-by-point basis at the well log and/or core scale. The scale of seismic data may exceed that of well log data by two or three orders of magnitude. A seismic wave tends to average the small-scale reservoir elastic features observed at a smaller scale. Sharp impedance and Poisson's ratio contrasts that manifest the presence of gas hydrate and free gas become smaller and may even disappear in impedance inversion volumes.

Consider a gas hydrate pseudo-well where the upper part of the sand body is filled with methane hydrate and the lower part contains free gas (Figure 20). The hydrate-cemented sand is manifested by large impedance while the sand with free gas is manifested by small Poisson's ratio.
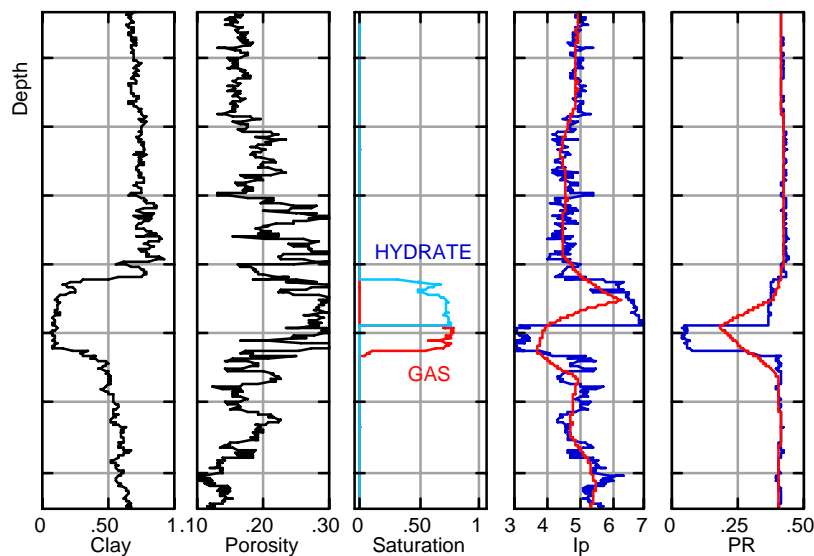


Figure 20. Pseudo well with methane hydrate. From left to right: clay content; total porosity; hydrate and gas saturation; P-wave impedance; and Poisson's ratio. The impedance and PR are calculated from porosity, clay content, and saturation according to the gas hydrate model. In the last two frames the blue curves are for the original log data while the red curves represent Backus average upscaling.

The smoothing effect of the seismic wave on the elastic attributes (upscaling) simulated via Backus averaging of the elastic moduli is displayed in Figure 21. The sharp impedance and PR contrasts apparent at the log scale become smaller. Even the vertical positions of the extrema of the upscaled elastic properties change.

Figure 21. Impedance versus PR from log data shown in Figure 20. Left: the original log data with the hydrate sand shown in blue and gas sand shown in red. Right: upscaled data with the hydrate sand in green and gas sand in yellow.

Because of the often complex stratigraphic distribution and thickness of sand/shale layers, there is no universal recipe for upscaling rock physics models and relations. The upscaling effect has to be assessed in each concrete case by synthetic seismic modeling or Backus averaging.
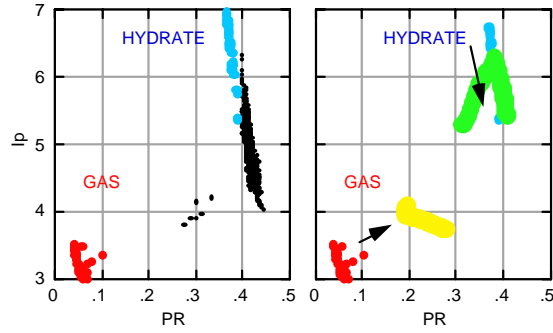
## CONCLUSION

The use of a first-principle-based rock physics model is crucial for gas hydrate reservoir characterization because only within a physics-based framework can one systematically perturb reservoir properties to estimate the elastic response with the ultimate goal of characterizing the reservoir from field elastic data. Rock physics relations have to be upscaled to become applicable to seismic reservoir characterization.

## WHAT NEEDS TO BE DONE

The state-of-the-art review above shows that several approaches have been used to derive methane hydrate concentration in-situ from seismic data. We believe that the physically consistent micromechanical model described in detail in this document can be successfully used in various depositional environments to detect and quantify methane hydrate reservoirs. In order to further validate this model we have to verify it by high-quality well log data from various locations worldwide. In order to make this model usable with seismic data we have to understand the issues of seismic resolution and how rock physics can be used with realistic, often uncalibrated, seismic impedance. We need

33

to understand how to use rock physics in various depositional settings where the methane hydrate reservoir has various elastic background (like shale at different degree of compaction) and also free gas underneath.

## APPROACH

Our approach is via rigorous forward modeling of the seismic signatures of methane hydrate using rock physics and validation of this modeling by real seismic data. An example of this approach and deliverables is shown in Figures 22 to 25 which is a snapshot of an applet which can be used by the geophysicist to assess reflection between shale and methane hydrate reservoir.
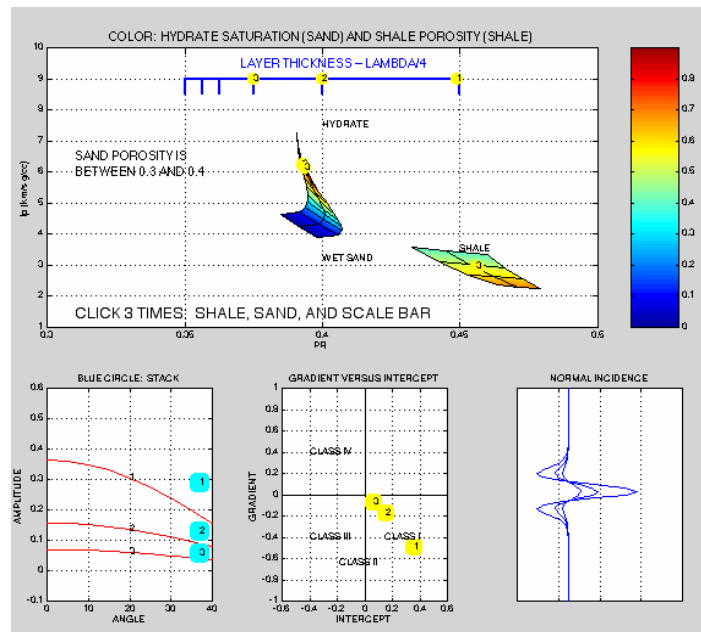


Figure 22. Half-space reflection modeling. The effect of hydrate saturation for thick sand thickness. The first (larger-amplitude) waveform is for the interface between shale and very thick sand with methane hydrate. The progressively smaller waveforms are for sand whose thickness is 1/8 and 1/16 of the wavelength. The first frame in the bottom row shows the corresponding AVO curves and amplitude stacks. This picture is a snapshot of an applet designed to assess the reflection at the interface between shale and sand with methane hydrate depending on the porosity and clay content in the shale; porosity in the sand; and methane hydrate saturation in the sand. The user has to first click in the colored shale domain, then in the sand, and, finally, on the scale bar to specify the thickness of the sand layer in terms of quarter-wavelength. The output is the AVO curve for each of three clicks, corresponding gradient versus intercept, and the waveform using a zero-phase Ricker wavelet.
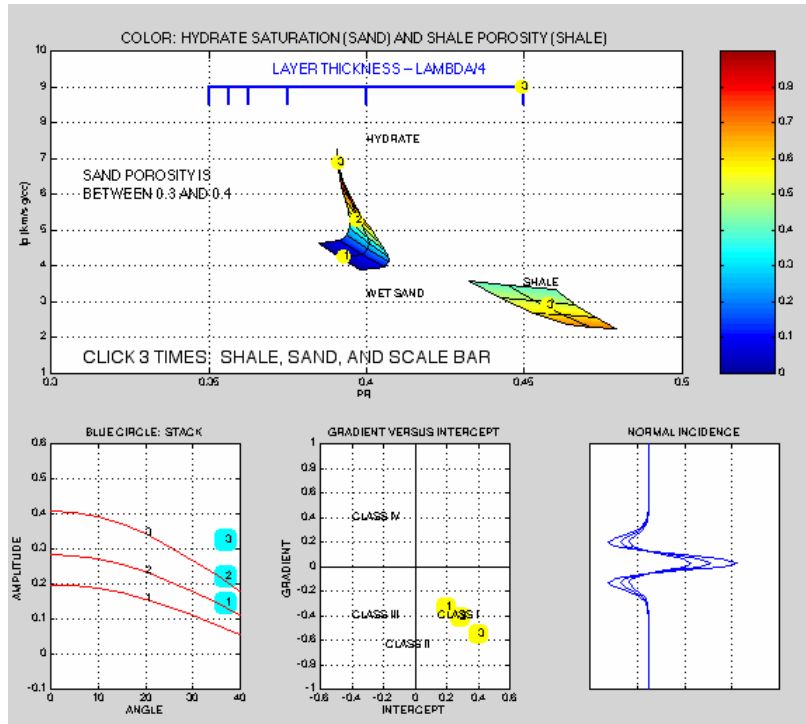
Figure 23. Half-space reflection modeling. The effect of hydrate saturation for thick sand.
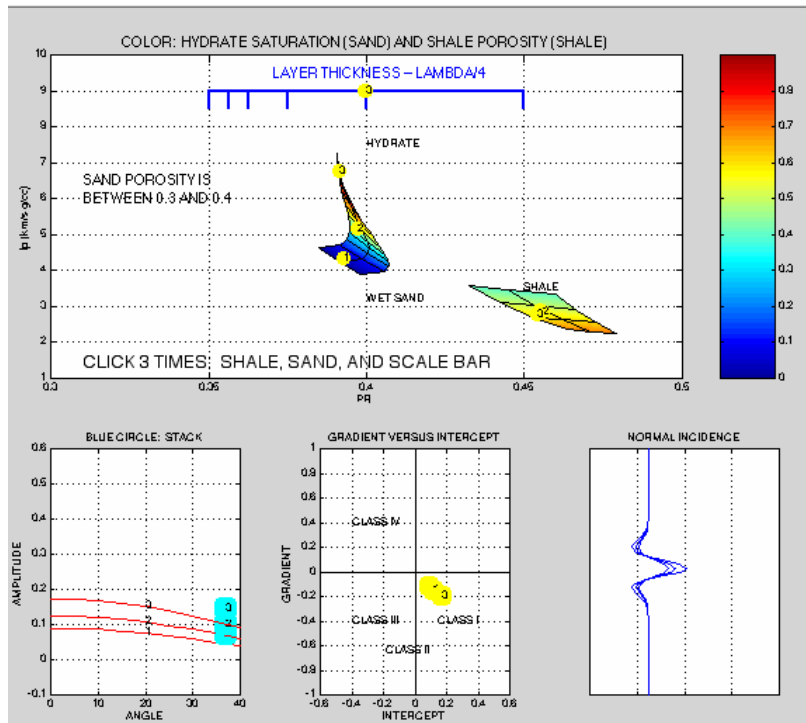


Figure 24. Half-space reflection modeling. The effect of hydrate saturation for thinner (1/8-wavelength) sand.
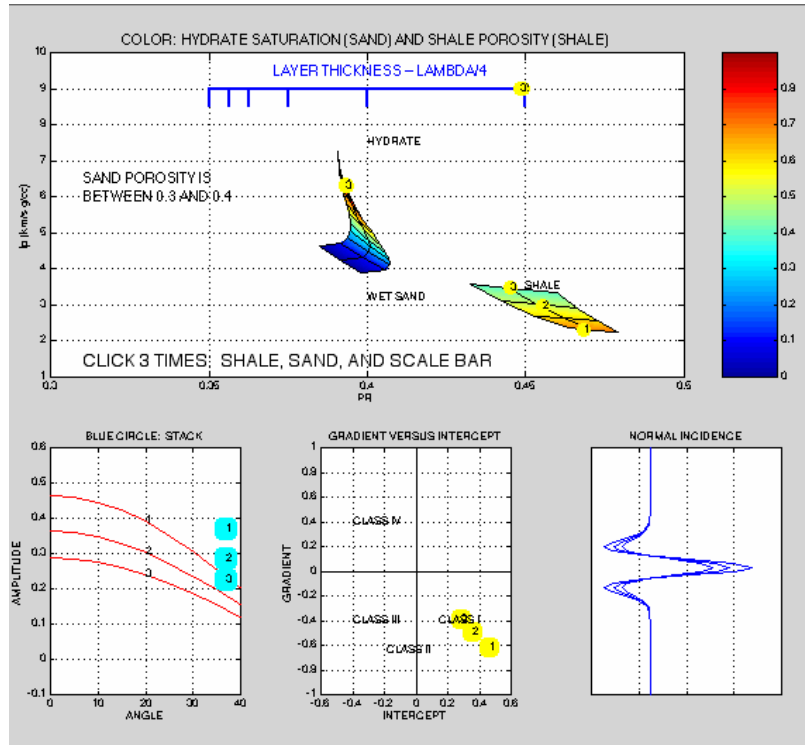
Figure 25. Half-space reflection modeling. The effect of shale porosity for reflection at thick sand.

## REFERENCES

Avseth, P., Dvorkin, J., Mavko, G., and Rykkje, J., 2000, Rock physics diagnostic of North Sea sands: Link between microstructure and seismic properties, GRL, 27, 2761-2764.

Bangs, N. L., D. S. Sawyer and X. Golovchenko, 1993, Free gas at the base of the gas hydrate zone in the vicinity of the Chile triple junction, Geology, 21, 905-908.

Batzle, M., and Wang, Z., 1992, Seismic properties of pore fluids, Geophysics, 57, 1396-1408.

Bunz, S., Mienert, J., Vanneste, M., and Andreassen, K, 2005, Gas hydrates at the Storegga Slide: Constraints from an analysis of multicomponent, wide-angle seismic data, Geophysics, 70, B19-B34.

Carcione, J.M., and Tinivella, U., 2000, Bottom-simulating reflectors: Seismic velocities and AVO effects, Geophysics, 65, 54–67.

Collins, B.P., and Watkins, J.S., 1985, Analysis of a gas hydrate off southwest Mexico using seismic processing techniques and Deep Sea Drilling Project Leg 66 results,

Geophysics, 50, 16-24.

Dai, J., Xu, H., Shyder, F., and Dutta, N.., 2004, Detection and estimation of gas hydrates using rock physics and seismic inversion: Examples from the northern deepwater Gulf of Mexico, The Leading Edge, 23, 60-66.

Dickens, G. D., C. K. Paull, and P. Wallace, 1997, Direct Measurement of in situ methane quantities in a large gas hydrate reservoir, Nature, 385, 426-428.

Dvorkin, J., and Nur, A., 1993, Rock Physics for Characterization of Gas Hydrates, in The Future of Energy Gases, USGS Publications, 293-298.

Dvorkin, J., Nur, A., and Yin, H., 1994, Effective Properties of Cemented Granular Materials, Mechanics of Materials, 18, 351-366.

Dvorkin, J., and Nur, A., 1996, Elasticity of high-porosity sandstones: Theory for two north sea datasets, Geophysics, 61, 1363-1370.

Dvorkin, J., 1996, Large Strains in Cemented Granular Aggregates: Elastic-Plastic Cement, Mechanics of Materials, 23, 29-44.

Dvorkin, J., and Nur, A., 1998, Time-Average Equation Revisited, Geophysics, 63, 460-464.

Dvorkin, J., Prasad, M., Sakai, A., and Lavoie, D., 1999, Elasticity of marine sediments, GRL, 26, 1781-1784.

Dvorkin, J., Nur, A., Uden, R., and Taner, T., 2003, Rock physics of gas hydrate reservoir, The Leading Edge, 22, 842-847.

Dvorkin, J., and Uden, R., 2004, Seismic wave attenuation in a methane hydrate reservoir, The Leading Edge, 23, 730-734.

Dvorkin, J., Helgerud, M., Waite, W., Kirby, S., and Nur, A., 2000, Introduction to physical properties and elasticity models, in Natural Gas Hydrate in Oceanic and Permafrost Environments, M.D. Max, ed., 245-260.

Ecker, C., Dvorkin, J., and Nur, A., 1998, Sediments with Gas Hydrates: Internal Structure from Seismic AVO, Geophysics, 1659-1669.

Ecker, C., Dvorkin, J., and Nur, A., 2000, Estimating the amount of gas hydrate and free gas from marine seismic data, Geophysics, 65, 565-573.

Gassmann, F., 1951, Elasticity of porous media: Uber die elastizitat poroser medien:

Vierteljahrsschrift der Naturforschenden Gesselschaft, 96, 1-23.

Guerin, G., Goldberg, D., and Meltzer, A., 1999, Characterization of in-situ elastic properties of gas-hydrate-bearing sediments on the Blake Ridge, JGR, 104, 17781-17796.

Guerin, G., and Goldberg, D., 2002, Sonic waveform attenuation in gas-hydrate-bearing sediments from the Mallik 2L-38 research well, Mackenzie Delta, Canada, JGR, 107, 1029-1085.

Helgerud, M., Dvorkin, J., Nur, A., Sakai, A., and Collett, T., 1999, Elastic-wave velocity in marine sediments with gas hydrates: Effective medium modeling, GRL, 26, 2021-2024.

Hill, R., 1952, The elastic behavior of crystalline aggregate, Proc. Physical Soc., London, A65, 349-354.

Holbrook, W. S., H. Hoskins, W. T. Wood, R. A. Stephen, D. Lizarralde, 1996, Methane Hydrate and Free Gas on the Blake Ridge from Vertical Seismic Profiling, Science, 273, 1840-1843.

Hyndman, R. D. and G. D. Spence, 1992, A Seismic Study of Methane Hydrate Marine Bottom Simulating Reflectors, JGR, V97, 6683-6698.

Kvenvolden, K. A., 1993, Gas Hydrates as a Potential Energy Resource–A Review of Their Methane Content, USGS Prof. Paper 1570, p. 555-561.

Lee, M.W., Hutchinson, D.R., Collett, T.S., and Dillon, W.P., 1996, Seismic velocities for hydrate-bearing sediments using weighted equation, JGR, 101, 20,347-20,358.

Lee, M.W., and Collet, T.S., 2001, Elastic properties of gas hydrate-bearing sediments, Geophysics, 66, 763-771.

Lee, M.W., 2002, Biot-Gassmann theory for velocities of gas hydrate-bearing sediments, Geophysics, 67, 1711-1719.

Lu, S., and McMechan, G.A., 2002, Estimation of gas hydrate and free gas saturation, concentration, and distribution from seismic data, Geophysics, 67, 582-593.

Mavko, G., T. Mukerji, J. Dvorkin, 1998, The Rock Physics Handbook: Tools for Seismic Analysis in Porous Media, Cambridge University Press, New York, 329.

Minshull, T. A., Singh, S.C., and Westbrook, G.K., 1994, Seismic velocity structure at a

gas hydrate reflector, offshore western Colombia, from full waveform inversion, JGR, 99, 4715-4734.

Miller, J. J., M. W. Lee and R. von Huene, 1991, An analysis of a Seismic Reflection from the base of a gas hydrate zone, offshore Peru, AAPG Bull., 75, 910-924.

Mindlin, R. D., 1949, Compliance of elastic bodies in contact, Trans. SDME, 71, A-259.

Nur, A., Mavko, G., Dvorkin, J., and Galmudi, D., 1998, Critical Porosity: A Key to Relating Physical Properties to Porosity in Rocks, The Leading Edge, 17, 357-362.

Koesoemadinata, A.P, and McMechan, G.A., 2001, Empirical estimation of viscoelastic seismic parameters from petrophysical properties of sandstone, Geophysics, 66, 1457-1470.

Matsushima, J., 2004, Attenuation measurements from sonic waveform logs in gas hydrate bearing sediments, Extended Abstract, SEG 74 Annual Meeting, Denver.

Pearson, C., J. Murphy and R. Hermes, 1986, Acoustic and Resistivity Measurements on Rock Samples Containing Tetrahydrofuran Hydrates: Laboratory Analogues to Natural Gas Hydrate Deposits, JGR, 91, 14132-14138.

Paull, C.K., Matsumoto, R., Wallace, P.J., et al., 1996. Proc. ODP, Init. Repts., 164: College Station, TX (Ocean Drilling Program).

Pratt, R.G., Bauer, K., and Weber, M., 2003, Cross-hole waveform tomography velocity and attenuation images of arctic gas hydrates, Expanded Abstract, SEG International Exposition and Seventy-Third Annual Meeting.

Prasad, M., and Dvorkin, J., 2001, Velocity to porosity transform in marine sediments, Petrophysics, 42, 5, 429-437.

Pride, S.R., Harris, J.M., Johnson, D.L., Mateeva, A., Nihei, K.T., Nowack, R.L., Rector, J.W., Spetzler, H., Wu, R., Yamamoto, T., Berryman, J.G., and Fehler, M., 2003, Permeability dependence of seismic amplitudes, TLE, 22, 518-525.

Reister, D., 2003, Using measured velocity to estimate gas hydrates concentration, Geophysics, 68, 884-891.

Reuss, A., 1929, Berechnung der Fliessgrenzev von Mischkristallen auf Grund der Plastizitätsbedingung für Einkristalle, Zeitschrift für Angewandte Mathematik und Mechanik, 9, 49-58.

Sakai, A., Velocity analysis of vertical seismic profiling (VSP) survey at Japex/JNOC/GSC Mallik 2L-38 gas hydrate research well, and related problems for estimating gas hydrate concentration, 1999, GSC Bulletin, 544, 323-340.

Scholl, D. W. and P. E. Hart, 1993, Velocity and Amplitude Structures on Seismic-Reflection Profiles–Possible Massive Gas-Hydrate Deposits and Underlying Gas Accumulations in the Bering Sea Basin, USGS Professional Paper 1570, 331-351.

Tinivella, U., and Carcione, J.M., 2001, Estimation of gas-hydrate concentration and free-gas saturation from log and seismic data, TLE, 20, 200-203.

Waite, W. F., M. B. Helgerud, A. Nur, J. Pinkston, L. Stern, S. Kirby and B. Durham, 1998, First Measurements of P- and S-Wave Speed on Pure Methane Gas Hydrate (abstract), EOS Transactions Suppl., 79, F463.

Wood, A.B., 1941, A textbook of sound, G. Bell and Sons, Ltd., London.

Wood, W. T., P. L. Stoffa and T. H. Shipley, 1994, Quantitative detection of methane hydrate through high-resolution seismic velocity analysis, JGR, 99, 9681-9695.

Wyllie, M.R.J., Gregory, A.R., and Gardner, L.W., 1956, Elastic wave velocities in heterogeneous and porous media, Geophysics, 21, 41-70.

Wood, W.T., Holbrook, W.S., and Hoskins, H., 2000, In situ measurements of P-wave attenuation in the methane hydrate–and gas-bearing sediments of the Blake Ridge, in Proceedings of the ODP, Scientific Results, 164, Paull, C.K., Matsumoto, R., Wallace, P.J., and Dillon, W.P. (Eds.), 265-271.

Wyllie, M.R.J., Gregory, A.R., and Gardner, L.W., 1956, Elastic wave velocities in heterogeneous and porous media, Geophysics, 21, 41-70.

Xia, G, Sen, M.K., and Stoffa, P.L., 2000, Mapping of elastic properties of gas hydrates in the Carolina trough by waveform inversion, Geophysics, 65, 735–744.